# Nanoscale

Accepted Manuscript


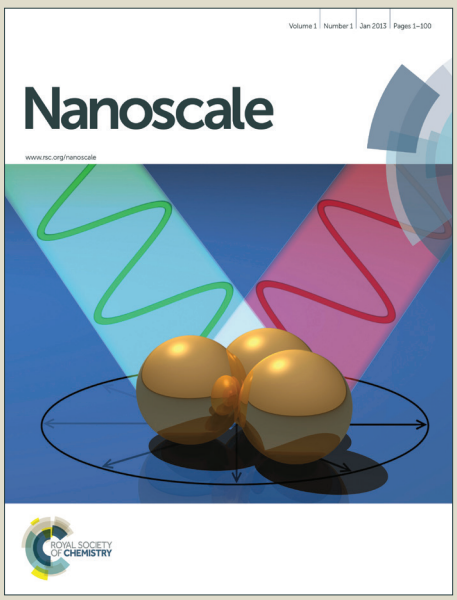





ROYAL SOCIETY OF CHEMISTRY

www.rsc.org/nanoscale

# Insight into Factors Affecting the Presence, Degree, and Temporal Stability of Fluorescence Intensification on ZnO Nanorod Ends

*Manpreet Singh†, Ruibin Jiang‡, Heidi Coia†, Daniel S. Choi†, Anginelle Alabanza†, Jae Young Chang†, Jianfang Wang‡, and Jong-in Hahm†**

†*Department of Chemistry, Georgetown University, 37th & O Sts. NW., Washington, DC, 20057 USA.*

‡*Department of Physics, The Chinese University of Hong Kong, Shatin, Hong Kong SAR, CHINA.*

**Address Correspondence to jh583@georgetown.edu*

## ABSTRACT

We have carried out a combined experimental and simulation study identifying the key physical and optical parameters affecting the presence and degree of fluorescence intensification measured on zinc oxide nanorod (ZnO NR) ends. Previously, we reported on the highly localized, intensified, and prolonged fluorescence signal measured on the NR ends, termed as fluorescence intensification on NR ends (*FINE*). As a step towards understanding the mechanism of *FINE*, the present study aims to provide an insight into the unique optical phenomenon of *FINE* through experimental and simulation approaches and to elucidate the key factors affecting the occurrence, degree, and temporal stability of *FINE*. Specifically, we examined the effect of the length, width, and growth orientation of single ZnO NRs on the NR-enhanced biomolecular emission profile after decorating the NR surfaces with different amounts and types of fluorophore-coupled protein molecules. We quantitatively and qualitatively profiled the biomolecular fluorescence signal from individual ZnO NRs as a function of both position along the NR long axis and time. Regardless of the physical dimensions and growth orientations of the NRs, we confirmed the presence of *FINE* from all ZnO NRs tested by using a range of protein concentrations. We also showed that the manifestation of *FINE* is not dependent on the spectroscopic signatures of the fluorophores employed. We further observed that the degree of *FINE* is dependent on the length of the NR with longer NRs showing increased levels of *FINE*. We also demonstrated that vertically oriented NRs exhibit much stronger fluorescence intensity at the NR ends and a higher level of *FINE* than the laterally oriented NRs. Additionally, we employed finite-difference time-domain (FDTD) methods to understand the experimental outcomes and to promote our understanding of the mechanism of *FINE*. Particularly, we utilized the electrodynamic simulations to examine both near-field and far-field emission characteristics when considering various scenarios of fluorophore locations, polarizations, spectroscopic characteristics, and NR dimensions. Our efforts may provide a deeper insight into the unique optical phenomenon of *FINE* and further be beneficial to highly miniaturized biodetection favoring the use of single ZnO NRs in low-volume and high-throughput protein assays.

## INTRODUCTION

Fluorescence has become one of the most commonly applied detection mechanisms in basic biology, applied medical research, and clinical diagnostics.[1,2] Hence, significant research efforts have been made in the past to improve the detection capability of biomolecular fluorescence signal. A considerable part of recent efforts has focused on engineering support materials that allow for better signal detection of proximal fluorophores that are conjugated to the biomolecules under investigation and subsequently placed on the support surfaces.[3-9] In particular, zinc oxide nanorods (ZnO NRs) have emerged as effective biomolecular fluorescence enhancing platforms whose applications in highly sensitive biodetection have been demonstrated in recently developed fluorescence-based assays for DNA sequence,[3,10-12] cytokine,[13] telomerase,[14] and other biomarker detection.[4,15,16]

ZnO NR platforms satisfy several key criteria to serve as promising supports for solid-state detection. ZnO NRs enable ultra-trace level biomolecular detection for various commonly employed fluorophores in the visible range regardless of their spectroscopic characteristics. At the same time, the enhanced biomolecular fluorescence detection capability of ZnO NRs is attained without the constraint of placing fluorophores at an optimal distance away from the support surfaces. Highly crystalline ZnO NRs are also fluorescence-free in the spectral range of visible (VIS) to near infrared (NIR) where most bioassay fluorophores exhibit absorption and emission. Therefore, ZnO NRs can function as detection platforms with no autofluorescence, and their use can facilitate accurate analyses of the measured fluorescence contributed only from the bioconstituents of interest.[11,12,15] To realize these advantages, periodic arrays of densely grown NRs have been synthesized and employed for most of the previously reported ZnO NR applications in biodetection. In these platforms, tightly packed, vertically oriented ZnO NRs were configured in pre-determined microarray patterns. Ensembles of ZnO NRs were then collectively used to detect the fluorescence signal derived from fluorophore-conjugated biomolecules on each detectable spot in the microarrays.[4,10,13,14]

In recent years, array technology has seen trends towards increased miniaturization from the micro-regime to the nanoscale.[17-20] Future applications of ZnO NRs may accordingly favor the use of single

ZnO NRs as distinct detection elements rather than ZnO NR ensembles, especially for *in vivo* imaging[21] and *in vitro* assays[11,12,15] requiring extremely low-volume and high-throughput analyses. Before such miniaturization can be fully realized, however, there is a critical need to probe individual ZnO NRs discretely since individual materials may possess substantially different optical behaviors than their ensemble-averaged response, as has been reported for single and multiple quantum dot systems.[22,23] Understanding the optical profiles of the individual nanomaterials collectively contributing to the enhanced spot signal can furthermore provide a basis for accurate signal processing and interpretation. These efforts can also initiate an exploration into newfangled characteristics associated with single nanostructures.

To this end, we have previously shown an intriguing phenomenon of fluorescence intensification on nanorod ends (*FINE*) observed from fluorophore/protein-coupled individual ZnO NRs.[24] This recent work signifies the first study to identify *FINE* by resolving photostability and fluorescence intensity on single ZnO NRs. However, the exact origins and mechanisms governing *FINE* are not yet well understood. As a step towards understanding the mechanism of *FINE*, valuable insights into the unique optical phenomenon of *FINE* need to be provided by elucidating key nanomaterial/biomolecular factors affecting the occurrence, degree, and temporal stability of *FINE*. Hence, a comprehensive investigation that qualitatively and quantitatively correlates the precise effect of important parameters such as the growth orientations of ZnO NRs, the physical dimensions of ZnO NRs, the use of different fluorophores, and the fluorophore/protein concentrations on the presence/degree of *FINE* is still highly warranted. As ZnO NR biosensing applications can utilize both vertically and laterally oriented rods of different aspect ratios for coupling with a mixture of fluorophores of various concentrations for multiplexing, it is important to examine how the aforementioned factors affect the spatial and temporal optical profiles of adsorbed biomolecules on different facets of individual ZnO NR crystals grown in different orientations. At the same time, any relationships between the presence/degree of *FINE* and the key nanomaterial/biomolecular factors should be unambiguously determined through combined experimental and simulation approaches.

Accordingly, we herein examine the emission profile and stability of various concentrations of immunoglobulin G antibody molecules that are coupled with either dichlorotriazinylaminofluorescein (DTAF-antiIgG) or tetramethylrhodamine isothiocyanate (TRITC-antiIgG) on individual ZnO NRs of specific growth orientations and physical dimensions. We then elucidate the effects of the NR orientations/dimensions and the dye concentrations/spectroscopic signatures on the degree of *FINE* as well as on the spatial and temporal fluorescence emission characteristics along the length of individual ZnO NRs. ZnO NRs varying in diameters and lengths are produced in two different growth orientations which are vertically out of and laterally within the nucleation plane of the NRs. We investigate the degree to which the physical dimensions and the two different orientations of ZnO NRs affect the highly localized optical phenomenon of *FINE*. When probing the degree of fluorescence enhancement and stability in these configurations, the DTAF- and TRITC-antiIgG emission signal is monitored distinctively from the end and side planes of single ZnO NRs at varying dye concentrations. Additionally, a finite-difference time-domain (FDTD) method is employed to understand our experimental observations and the origin of *FINE*. Understanding such relationships will provide fundamental knowledge beneficial for *in vivo* measurements and *in vitro* applications using single ZnO NRs.

Our key findings from these experimental and FDTD simulation efforts are multifold. When profiling the signal distribution across the long axis of individual ZnO NRs, highly localized signal intensification is monitored at the NR end planes relative to the side planes, irrespective of ZnO NR orientation and dimension. The observation of *FINE* also does not appear to have any dependence on the spectroscopic profiles of the fluorophores employed. The degree of *FINE* is enhanced with increasing NR length whereas NR width does not seem to play a significant role. The degree of *FINE* is also increased with higher protein concentration. Vertically oriented ZnO NRs show a much greater degree of *FINE* when compared to ZnO NRs oriented laterally, regardless of the fluorophore's concentration or spectroscopic property. The photostability of the biomolecular fluorescence signal observed from NR end facets is higher than that from NR side facets. Our results are anticipated to provide a basis for signal

interpretation of fluorescence-based biodetection involving individual ZnO NRs as well as ensembles. The distinctive biomolecular emission profiles characterized for the different ZnO NR crystalline planes and growth orientations may promote innovative biomedical applications based on the use of single ZnO NRs by harnessing their unique shape anisotropy for highly directional and locally enhanced optical detection.

## EXPERIMENTAL SECTION

Isolated ZnO nanorods were synthesized in a home-built chemical vapor deposition reactor. The source materials, 0.45 grams of a 2:1 mixture of graphite (99%) to zinc oxide powder (99.999%) obtained from Alfa Aesar Inc., were placed on a quartz boat at the center of a horizontal resistance furnace. The growth substrate, a 1 x 1 cm Si wafer (0.432 mm in thickness) obtained from Silicon Quest International, Inc. (San Jose, CA), was ultrasonically cleaned in ethanol and placed on a target quartz boat 15.6 cm away from the source boat, downstream from the carrier gas flow. Growth of L-ZnO NRs was achieved by pretreating the Si wafer with 20 μL of 20 nm Au colloid (Ted Pella, Inc.) for 5 min and gently drying with $N_2$. To achieve V-ZnO NRs, catalyst delivery was carried out by microcontact printing the Au nanoparticles on the growth substrate using a poly-L-lysine treated polydimethylsiloxane (PDMS) stamp containing periodic 10 x 10 μm square patterns. The source boat was subsequently heated to 950 °C for 20 min to 1 h at a ramp-up/ramp-down rate of 15 °C $min^{-1}$ under a constant Ar flow of 100 standard cubic centimeters per minute. For characterization of morphology, as-grown ZnO NRs were imaged using a FEI/Philips XL 20 SEM operating at 20 kV.

For biomolecule treatment of the NRs, TRITC-antiIgG and DTAF-antiIgG were received from KPL, Inc. and Rockland Immunochemicals, Inc., respectively. Both TRITC-antiIgG and DTAF-antiIgG were reconstituted as per manufacturing recommendations and further diluted in deionized water (DI). The ZnO platforms were incubated with 10 μL of varying concentrations of each fluorophore-coupled

protein, protected from light, and placed in humidity controlled chamber for 5 min. The substrate was subsequently washed twice using 40 μL aliquots of DI, dried under a gentle stream of $N_2$, and immediately imaged. Post-imaging, substrates were cleaned by exposure to $N_2$ plasma for 5 min under vacuum in a Harrick PDC-32G plasma cleaner at a setting of 18 W radio frequency for removal of the biomolecules.

For all optical measurements, a Zeiss Axio Imager A2M (Carl Zeiss, Inc., Thornwood, NY) microscope equipped with an AxioCAM HRm digital camera was employed. Reflected bright-field illumination and unpolarized fluorescence excitation were produced using a 12V/100 W halogen lamp and a 120 W mercury vapor lamp (X-Cite 120Q), respectively. For TRITC-antiIgG (DTAF-antiIgG), a spectroscopic setting of 540-552 nm (450-490 nm) excitation and 575-640 nm (510-540 nm) collection was employed along with a 560 nm (495 nm) long-pass filter to ensure collection of only the biomolecular emission. Samples were subjected to 10 min of constant irradiation in a darkroom and imaged periodically using a 2 sec exposure and an EC Epiplan-NEOFLUAR 50X magnification (numerical aperture, NA = 0.8) objective lens. The uncompressed time-lapse images were exported from AxioVision to the Java-based image-processing program, Image J, for analysis and subsequent signal quantification was conducted using Origin 8 software (OriginLab Corp.).

All simulations were performed using FDTD Solution 8.7 (Lumerical Solutions, Inc.). The nanostructure and its surrounding medium were divided into meshes of 3 nm in size. The refractive indexes of the surrounding medium and ZnO were taken to be 1 and 1.95,[25] respectively. The ZnO NR was modeled as a hexagonal prism while changing its width and length. In order to simulate the case of TRITC-antiIgG (DTAF-antiIgG) while accounting for the physical size of the protein, an electric dipole with the radiation wavelength of 576 nm (517 nm) was placed on the middle or at the end of the NR, 10 nm away from the NR surface.

## RESULTS AND DISCUSSION

**I. Nanomaterial and Biomolecular Factors Evaluated in *FINE* Analysis.** To aid in the discussion of our measurements in this paper, we first define the end and side crystalline facets of a ZnO NR. The NRs employed in our investigation expose basal planes on the two NR ends and prismic planes on their six sides. Hence, the end and side facets of the ZnO NR are herein referred to as ZnO $NR_{ef}$ and ZnO $NR_{sf}$, respectively. We further differentiate the growth orientations of the NRs as lateral (L-ZnO NR) and vertical (V-ZnO NR) with respect to the NR nucleation plane, as shown schematically in the top panel of Fig. 1(A). In Fig. 1(B), typical reflected bright-field (BF) images of the as-grown ZnO NR(s) are provided to visualize the NR platforms prior to biodeposition and fluorescence imaging. The left microscopic image displays a laterally grown ZnO NR whose entire length lies within the imaging focal plane, whereas the right BF image presents the end facets of vertically grown NRs by focusing onto the free-standing NR tips. In addition, characteristic scanning electron microscopy (SEM) images of a typical, as-grown ZnO NR are provided in Fig. 1(C). As represented, the wurzite, single crystal ZnO NRs utilized in our study reveal two well-defined hexagonal end facets exposing the basal planes in addition to six rectangular side facets around the main body displaying the prismic planes, defined earlier as ZnO $NR_{ef}$ and ZnO $NR_{sf}$, respectively.

Post-synthesis, ZnO NRs of both orientations were subsequently treated with different fluorophore-coupled biomolecules in order to examine systematically the biomolecular fluorescence signal. The two model fluorophores selected for coupling and profiling, TRITC-antiIgG and DTAF-antiIgG, display emission in the red (r) and green (g) spectral regions, respectively. The signal was collected both spatially, as a function of position along the NR length, and temporally, as a function of time. Note that the collected signal is emitted by the fluorophores, not from the bandgap emission of the NRs which is in the UV range. The excitation/collection wavelengths in our investigation are in the VIS range tuned for the specific spectroscopic signatures of the two fluorophores. The signal intensity and stability were profiled on individual ZnO NRs with high crystallinity, varying aspect ratios, and well-defined growth orientations in order to elucidate the effect of the NR shape anisotropy, dimensions, and orientation on

the measured biomolecular fluorescence signal. This overall approach is schematically depicted in the bottom panel of Fig. 1(A) and systematically outlined in Fig. 1(D) with all relevant notations used throughout this paper. Due to the potential applications in biomedical detection, our investigation in this study utilizes fluorophore-tagged proteins instead of just fluorophores in the investigation of *FINE*. However, fluorophores used without being conjugated to any biomolecules also exhibit fluorescence signal intensification on ZnO NR ends.[24]

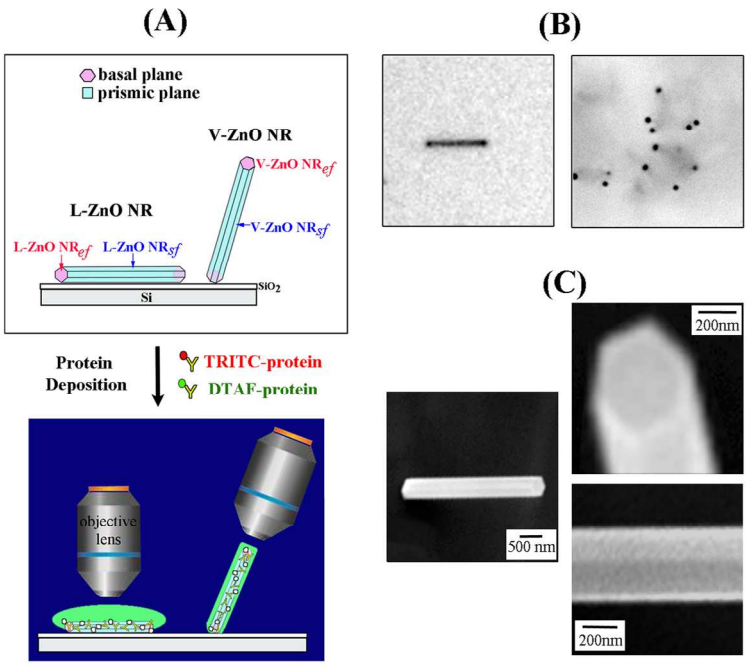


(D)

| Crystal Facets | Fluorophores coupled to Protein (emission color) | Growth Orientations | |
|---|---|---|---|
| | | Vertical | Lateral |
| ⬢ | DTAF (g) | V-ZnO NR*ef*,g | L-ZnO NR*ef*,g |
| | TRITC (r) | V-ZnO NR*ef*,r | L-ZnO NR*ef*,r |
| ▢ | DTAF (g) | V-ZnO NR*sf*,g | L-ZnO NR*sf*,g |
| | TRITC (r) | V-ZnO NR*sf*,r | L-ZnO NR*sf*,r |

**Figure 1. (A)** Schematic illustrations are presented to distinguish and define the growth orientations and NR end facets from the main body of the wurtzite ZnO NRs that were used for our biomolecular fluorescence investigation. Single ZnO NRs of lateral and vertical growth orientations were used for our study. In order to differentiate NRs of different growth directions with respect to the plane of an underlying silicon substrate, laterally and vertically grown ZnO NRs are referred to as L-ZnO NR and

V-ZnO NR, respectively. After coupling NRs with fluorophore-modified proteins of interest, characteristic emission behaviors of the biomolecules on individual ZnO NRs were monitored by using the excitation/emission properties of the fluorophore. Based on the emission color of the fluorophore, TRITC-antiIgG and DTAF-antiIgG are denoted as r (for red) and g (for green), respectively. The biomolecular emission monitored from the NR end and side facets is indicated as $NR_{ef}$ and $NR_{sf}$, respectively. **(B)** Reflected BF optical images shown display individual ZnO NRs grown laterally within (left) and vertically out of (right) the underlying growth wafer. In the BF image of the V-ZnO NRs, the dark dots are the basal planes of vertically grown ZnO NRs that are in the imaging focal plane. **(C)** The three SEM panels display the rectangular side facets and hexagonal end facets of a typical ZnO NR crystal. The displayed ZnO NR exhibits 390 nm in width and 2.95 μm in length. **(D)** The table contains various notations used throughout this paper to indicate the systematic measurement combinations of the two fluorophores with different crystalline facets and growth orientations of the ZnO NR.

**II. NR Orientation and Fluorophore Spectroscopic Property on *FINE*.** ZnO NR-enabled *FINE* was comprehensively examined by systematically analyzing the temporal fluorescence profiles of TRITC-antiIgG and DTAF-antiIgG on both L-ZnO NRs and V-ZnO NRs to obtain the degree of biomolecular signal difference measured from the end facets versus the main body of individual ZnO NRs. Specifically, for each NR orientation, the average emission signal from the end and side facets of individual ZnO NRs was carefully evaluated to differentiate the biomolecular fluorescence collected from L-ZnO $NR_{ef}$, L-ZnO $NR_{sf}$, V-ZnO $NR_{ef}$, and V-ZnO $NR_{sf}$. These results from our systematic temporal and spatial investigations are summarized qualitatively in Fig. 2 and quantitatively in both Fig. 3 and Table 1. In addition, the effect of the fluorophore's spectroscopic property on the presence of *FINE* was evaluated, and the qualitative results are shown in Fig. 2.

**DTAF-antiIgG on the Side and End Facets of L- versus V-ZnO NRs.** Displayed in Fig. 2(A) are typical biomolecular fluorescence panels capturing the emission of 5 μg/mL DTAF-antiIgG on an

individual L-ZnO NR (left) and V-ZnO NR (right). The BF images in the insets show the main body of a L-ZnO NR and the end facet of a single V-ZnO NR in the left and right panel, respectively. As seen by the L-ZnO NR, there is clear evidence of non-uniform distribution of the DTAF-antiIgG fluorescence signal along the length of the NR, indicating the presence of the previously elucidated, facet-dependent, optical phenomenon of *FINE*. In addition, we note that the 5 μg/mL DTAF-antiIgG fluorescence intensity from the V-ZnO $NR_{ef}$ is 1.82 times higher than that on L-ZnO $NR_{ef}$.

**TRITC-antiIgG on the Side and End Facets of L- versus V-ZnO NRs.** Fig. 2(B) presents time-lapse fluorescence panels displaying the temporal and spatial emission characteristics of 1 μg/mL TRITC-antiIgG on a L-ZnO NR (top) and a V-ZnO NR (bottom). We chose this model system in order to simultaneously understand the NR orientational factor on the degree of *FINE* and examine the effect of the fluorophore's spectroscopic property on the presence of *FINE*. The degree of *FINE* is defined as the enhancement level of the fluorescence signal collected from $NR_{ef}$ with respect to that measured from $NR_{sf}$. For the L-ZnO NR in the top panel of Fig. 2(B), strong TRITC-antiIgG emission at the two far ends of the NR can be clearly seen even at 10 min, at which point the fluorescence signal on the NR main body is substantially reduced and no longer clearly visible. This indicates that constant irradiation yields faster fluorescence decay from TRITC-antiIgG on the main body of the NR than from the NR ends. The degree of signal intensification in *FINE*, $(\boldsymbol{I}_{\mathrm{avg,NR}ef} - \boldsymbol{I}_{\mathrm{avg,NR}sf})/\boldsymbol{I}_{\mathrm{avg,NR}sf}$, was determined as 47% on average for the L-ZnO NR displayed. Similarly, in the bottom panel of Fig. 2(B), fluorescence characteristics of 1 μg/mL TRITC-antiIgG on a V-ZnO $NR_{ef}$ were captured by focusing on the tip of the protruding single ZnO NR. Considerably stronger fluorescence intensity was observed on the end facets of V-ZnO NRs than on the same facets of L-ZnO NRs exposed to identical biomolecular deposition conditions. When compared to the initial intensity at T = 0 sec measured on the L-ZnO $NR_{ef}$, the average fluorescence intensity of 1 μg/mL TRITC-antiIgG on the V-ZnO $NR_{ef}$ was five times higher. For the emission profiling of proteins on the V-ZnO $NR_{sf}$, the focal plane was adjusted to the middle of the NR main body at the midpoint between the growth wafer and the NR tip planes. Parallel to the

trends from both DTAF-antiIgG and TRITC-antiIgG on the two different facets of the L-ZnO NR, the biomolecular emission from the V-ZnO $NR_{ef}$ was much higher in intensity relative to the signal collected from the V-ZnO $NR_{sf}$.

**Fluorophore Spectroscopic Property and the Occurrence of *FINE*.** Although qualitatively visualized, results shown in Fig. 2 display clearly that the intensified fluorescence present on the two NR ends for the different fluorophore cases of DTAF (Emission $\lambda_{max}$ = 517 nm) and TRITC (Emission $\lambda_{max}$ = 576 nm). Therefore, the specific absorption/emission profiles of the fluorescent dyes employed do not appear to affect the occurrence of *FINE* in individual ZnO NRs.

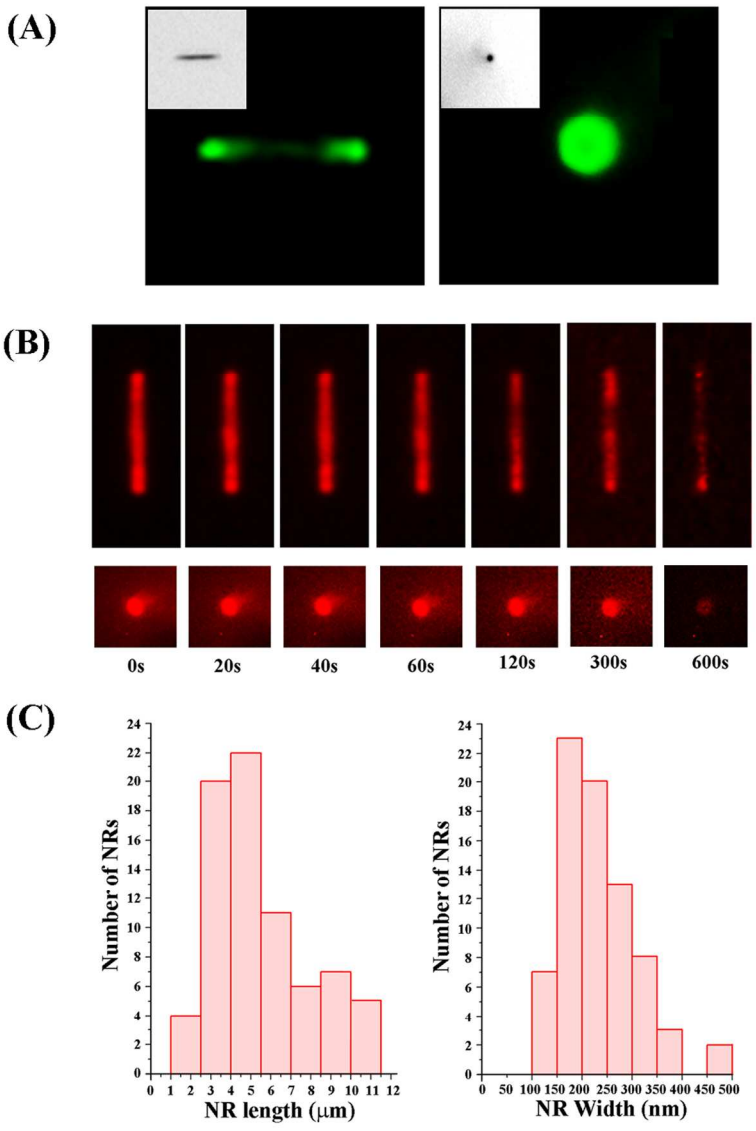

**Figure 2. (A)** Typical fluorescence panels collected at time zero, T = 0 sec, are displayed from a L-ZnO NR and a V-ZnO NR after deposition with 5 μg/mL DTAF-antiIgG. The insets are bright-field panels showing the entire body of a L-ZnO NR (left) and the tip of a V-ZnO NR (right) in the focal plane. In the BF image of the V-ZnO NR, the dark dot is the end facet exposing the basal plane of a vertically grown ZnO NR that was in the imaging focal plane. Brightness and contrast of the fluorescence panels were adjusted to show the *FINE* effect at the end facets of the L-ZnO NR (left) and the intense biomolecular emission collected from the NR end facet of the V-ZnO NR (right). **(B)** Time-lapse fluorescence panels of a L-ZnO NR (top) and a V-ZnO NR (bottom) from which the spatial and temporal emission behavior of 1 μg/mL TRITC-antiIgG were qualitatively observed. **(C)** Length and width histograms of the L-ZnO NRs used for the statistical analysis of fluorescence intensities on the protein-decorated $NR_{sf}$ and $NR_{ef}$ are provided.

**Further Look at NR Orientation and the Degree of *FINE*.** With regards to ZnO NR orientation, the degree of *FINE* is always much larger for V-ZnO NRs than for L-ZnO NRs. The V-ZnO NR shown in the bottom panels of Fig. 2(B) exhibited a $NR_{ef}/NR_{sf}$ fluorescence intensity ratio of 19 at T = 0 sec, whereas the L-ZnO NR shown in the top panels Fig. 2(B) displayed a much reduced $NR_{ef}/NR_{sf}$ value of 1.47. We denote fluorescence intensity as ***I***. We hypothesize that the origin of the significantly higher ratio of $\boldsymbol{I}_{\mathrm{avg,NR}ef} / \boldsymbol{I}_{\mathrm{avg,NR}sf}$ observed from V-ZnO NRs may be associated with two factors: the substrate effect and the signal collection angle. In the free standing NR orientation of V-ZnO NRs, fluorescence emitted from TRITC-antiIgG may be guided along the surface and medium of the ZnO NR more effectively than for L-ZnO NRs and subsequently permit enhanced far-field radiation from the NR tip due to minimized loss of the electromagnetic radiation through substrate coupling. The contact of L-ZnO NRs with the underlying substrate may serve as the main source of radiation loss when biomolecular fluorescence signal is being guided along the NR towards the NR ends. Similar substrate-induced reduction of optical signal has been previously reported in waveguides and lasers.[26-30] For

example, leaky loss through underlying substrates in thin film waveguides can be reduced by removing and replacing the substrate with a low-loss material during waveguide construction.[26] A similar trend of radiation loss induced by the substrate was also reported in whispering gallery mode lasing in ZnO nanodisks.[27] Tapered ZnO nanodisks, rather than those with flat bases, can be used to reduce the area of low-contrast index at the ZnO-substrate interface and thus, serve as reflectors by enabling a high index contrast barrier at the substrate interface. In addition to the contribution from the loss via substrate-contact, the collection angle of the fluorescence signal may also play a part in our observations of a higher degree of *FINE* for V-ZnO NRs relative to L-ZnO NRs. In our measurement configuration, where the detector is fixed at an angle above the sample plane, the far-field radiation emanating from the end facets can be more efficiently directed in space into the collection lens for the vertically arranged $NR_{ef}$ than the laterally placed $NR_{ef}$. In particular, the main emission axis from the $NR_{ef}$ for the V-ZnO (L-ZnO) case falls within (outside) the half angle defined by the numerical aperture of the lens as the NRs are standing out of (lying flat within) the sample plane. Hence, the increased degree of *FINE* observed from V-ZnO NRs relative to L-ZnO NRs in our study may also have originated from the better directional collection of the biomolecular emission.

**Occurrence Frequency and Possible Origins of *FINE*.** In Fig. 2(C), distributions in the lengths and widths of all L-ZnO NRs used for the statistical analyses of biomolecular fluorescence intensities are provided in the respective histograms. We repeatedly observed the phenomenon of *FINE* from a large number of ZnO NRs as shown in Fig. 2(C) where, within the experimental parameters of NR length/diameter and protein concentration/fluorophore type we tested, *FINE* was consistently observed from all NRs charted in Fig. 2(C). A majority of ZnO NRs used in our experiment exhibit an aspect ratio greater than 10:1 in length:width. When considering the total surface area of the two hexagonal end facets versus the six rectangular side facets for a typical NR with an aspect ratio of 10:1, a total surface area ratio of 30:1 ($NR_{sf}$: $NR_{ef}$) is expected. When assuming an equal preference of IgG binding to the two types of NR facets, the surface area ratio implies that the amount of proteins found on the NR side facets will be much greater than on the end facets due to a greater available surface area for protein

adsorption. The estimated protein number density ratio will be the same as 30:1 (on $NR_{sf}$ : on $NR_{ef}$) based on the available facet area for a full protein coverage. However, the average fluorescence intensity measured from $\boldsymbol{I}_{avg,NR_{ef}}$ in our experiments was always higher than $\boldsymbol{I}_{avg,NR_{sf}}$. It is also likely that proteins show a different degree of binding towards the two NR surfaces. The exact binding preference of IgG on different ZnO NR crystal facets is not known at the individual crystal level. Nonetheless, a few systems investigating facet-specific binding of enzymatic proteins on cellulose microfibril crystals, whose geometric shapes resemble those of one-dimensional ZnO NRs, reported that surface adsorption of proteins is favored on the side facets relative to the end facets of the microfibril crystals.[31,32] Despite that more proteins are expected on the NR side facets compared to the end facets based on the two factors of a larger surface area and a higher protein binding preference to the side facets, higher fluorescence signal is consistently observed from the $NR_{ef}$ than from the $NR_{sf}$ in all our measurements. Hence, the amount of proteins on different ZnO NR surfaces does not seem to have a considerable effect on the presence of *FINE*. Rather, the unique optical behavior of *FINE* observed from the ZnO NRs seems to have originated from the inherent material property of ZnO in reduced physical dimensions coupled with the high shape anisotropy which will be discussed later in depth with our simulation data.

**Temporal Stability of *FINE* and Photostability on Different NR Facets.** The phenomenon of ZnO NR-enabled *FINE* was systematically profiled further by quantitatively analyzing the temporal fluorescence profiles of TRITC-antiIgG and DTAF-antiIgG measured from the $NR_{ef}$ and $NR_{sf}$ regions for each NR orientation. These results are summarized in Fig. 3 and Table 1 for different concentrations of the two types of fluorophores investigated. In panels 3(A and B), the three-dimensional (3D) contour plots profile fluorescence intensity as a function of both time and position along the long axis of a L-ZnO NR for 10 μg/mL DTAF-antiIgG (A) and 1 μg/mL TRITC-antiIgG (B). As was qualitatively evidenced in Fig. 2, the highly localized fluorescence intensification from the two ZnO NR end facets relative to that along the NR main body is displayed in Figs. 3(A and B) for the cases of DTAF-antiIgG and TRITC-antiIgG, respectively. In Fig. 3(C and D), the time-dependent emission decay profiles of 10 μg/mL DTAF-antiIgG (C) and 1 μg/mL TRITC-antiIgG (D) on different positions of L- and V-ZnO

NRs are quantitatively revealed. In all time-dependent fluorescence intensity plots shown in Fig. 3, the signal is normalized with regards to the initial fluorescence intensity at T = 0 sec.

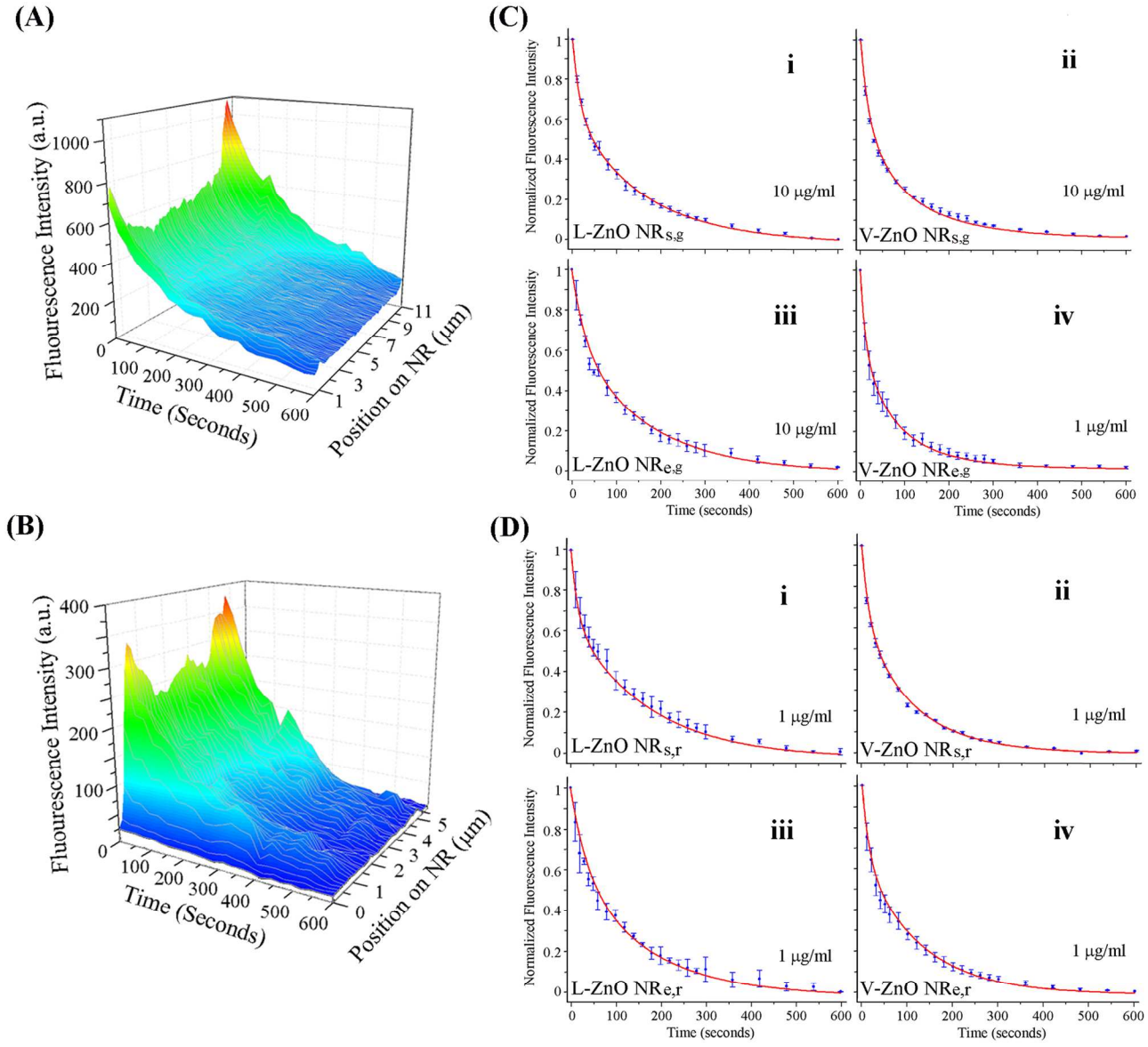


**Figure 3. (A and B)** The 3D contour plots display the spatial and temporal emission profile of 10 μg/mL DTAF-antiIgG (A) and 1 μg/mL TRITC-antiIgG (B) on single L-ZnO NRs. The contour plots quantitatively display the biomolecular fluorescence intensity of the L-ZnO NRs measured along the length of the NR over time. **(C)** Temporal stability of the fluorescence emission of 10 μg/mL DTAF-antiIgG was recorded on the main body (i) and end facets (iii) of individual L-ZnO NRs and plotted as a function of time. Similar photostability measurements were repeated on the main body (ii) and end

facets (iv) of individual V-ZnO NRs and plotted as a function of time. 10 μg/mL DTAF-antiIgG on the end facets of V-ZnO NRs led to signal saturation of the detector. Hence, concentrations of 10 and 1 μg/mL DTAF-antiIgG were used for the data shown in (ii) and (iv), respectively. **(D)** Similar temporal analyses for fluorescence intensity were carried out by using 1 μg/mL TRITC-antiIgG, and the results are presented based on the side and end facets of L- and V-ZnO NRs in the same arrangement as in (C). The time indicated with a black arrow in each graph in (C and D) indicates the respective half-life ($T_{1/2}$) when the fluorescence intensity is reduced to ½ of its original value at T = 0 sec.

We define $T_{1/2}$, $T_{1/5}$, and $T_{1/10}$ as the time taken for the fluorescence intensity to decline to 50%, 20%, and 10% of the initial intensity at T = 0 sec, respectively. The signal from DTAF-antiIgG on L-ZnO $NR_{ef}$ in Fig. 3(C-iii) showed more prolonged photostability and a longer half-life of $T_{1/2}$ = 63 sec, when compared to the signal from L-ZnO $NR_{sf}$ in Fig. 3(C-i) showing a half-life of $T_{1/2}$ = 43 sec. Due to detector saturation at 10 μg/mL concentrations of DTAF-antiIgG, the photostability panel shown in Fig. 3(C-iv) corresponding to the case of V-ZnO $NR_{ef}$ was from 1 μg/mL DTAF-antiIgG. Similar to the case of DTAF-antiIgG, the average half-life was extended from 49 sec to 60 sec for 1 μg/mL TRITC-antiIgG adsorbed on the L-ZnO $NR_{ef}$ in Fig. 3(D-iii) compared with the L-ZnO $NR_{sf}$ in Fig. 3(D-i). The increased photostability monitored on $NR_{ef}$ with respect to $NR_{sf}$ was evident not only for the aforementioned L-ZnO NRs but also for V-ZnO NRs, although the effect for V-ZnO NR was reduced relative to the case of L-ZnO NR. The fluorescence half-life on the V-ZnO $NR_{ef}$ in Fig. 3(D-iv) was also extended compared to that on the V-ZnO $NR_{sf}$ in Fig. 3(D-ii) from 35 sec to 40 sec, when the same biomolecular deposition conditions were used. Similar analyses were performed to determine $T_{1/5}$, and $T_{1/10}$ values. All photostability values were then catalogued based on the NR orientation, NR facet, fluorophore type, and protein concentration for quantitative comparison in Table 1. Regardless of the protein concentrations and types of fluorophore used, photostability was higher for V-ZnO $NR_{ef}$ (L-ZnO

$NR_{ef}$) with respect to V-ZnO $NR_{sf}$ (L-ZnO $NR_{sf}$), as larger $T_{1/2}$, $T_{1/5}$, and $T_{1/10}$ values were generally exhibited. However, the difference in fluorescence decay rates between $NR_{ef}$ versus $NR_{sf}$ of the same growth orientation decreased after $T_{1/2}$ and the exponential decay profiles of intensity changed slowly over time. Photochemical destruction of fluorophores resulting in signal reduction can impose a significant problem in many fluorescence-based biodetection techniques. For the concentration ranges of 1 μg/mL to 200 μg/mL we assayed, the photostability profiles do not exhibit substantial dependence on protein concentration and show much increased half-lives for all concentrations when compared to those of similar fluorophores in solution. Most organic fluorophores exhibiting molar extinction coefficients of 5-10 x $10^4$/(M•cm) typically have $T_{1/2}$ values shorter than 15 sec.[9,33-35] Considering this factor, the use of a ZnO NR platform extends the photostability of fluorophores considerably regardless of fluorophore type and protein concentration which, in turn, permits fluorescence detection of biomolecules via spatially localized, highly intense, and temporally prolonged signal.

| Dye-coupled Biomolecules | Test Platforms | $T_{1/2}$ (sec) | $T_{1/5}$ (sec) | $T_{1/10}$ (sec) |
|---|---|---|---|---|
| 200 μg/mL DTAF-antiIgG | V-ZnO $NR_{ef,g}$ | detector saturated | | |
| | V-ZnO $NR_{sf,g}$ | detector saturated | | |
| | L-ZnO $NR_{ef,g}$ | 60 ± 5.3 | 163 ± 10.1 | 250 ± 15.9 |
| | L-ZnO $NR_{sf,g}$ | 40 ± 6.0 | 136 ± 5.5 | 237 ± 17.4 |
| 200 μg/mL TRITC-antiIgG | V-ZnO $NR_{ef,r}$ | detector saturated | | |
| | V-ZnO $NR_{sf,r}$ | 49 ± 4.1 | 149 ± 8.6 | 229 ± 10.6 |
| | L-ZnO $NR_{ef,r}$ | 50 ± 8.2 | 188 ± 17.4 | 262 ± 23.2 |
| | L-ZnO $NR_{sf,r}$ | 35 ± 6.8 | 138 ± 16.7 | 225 ± 20.5 |
| 10 μg/mL DTAF-antiIgG | V-ZnO $NR_{ef,g}$ | detector saturated | | |
| | V-ZnO $NR_{sf,g}$ | 30 ± 2.9 | 120 ± 11.6 | 240 ± 20.5 |
| | L-ZnO $NR_{ef,g}$ | 63 ± 7.7 | 174 ± 10.8 | 250 ± 21.8 |
| | L-ZnO $NR_{sf,g}$ | 43 ± 4.5 | 170 ± 10.0 | 279 ± 20.4 |
| 1 μg/mL TRITC-antiIgG | V-ZnO $NR_{ef,r}$ | 40 ± 5.0 | 149 ± 12.1 | 220 ± 14.5 |
| | V-ZnO $NR_{sf,r}$ | 35 ± 3.0 | 130 ± 13.5 | 205 ± 10.4 |
| | L-ZnO $NR_{ef,r}$ | 60 ± 7.6 | 178 ± 18.3 | 282 ± 21.2 |
| | L-ZnO $NR_{sf,r}$ | 49 ± 7.7 | 180 ± 16.5 | 290 ± 12.6 |

**Table 1.** Averaged photostability characteristics of biomolecular fluorescence are profiled by listing $T_{1/2}$, $T_{1/5}$, and $T_{1/10}$ values for various single ZnO NR platforms. The photostability data were catalogued based on the two growth orientations of vertical (V) and lateral (L), the position of the NR end facet ($NR_{ef}$) and NR main body ($NR_{sf}$), and the two types of fluorophores of DTAF (g) and TRITC (r) at varying protein concentrations.

**Protein Concentration on *FINE*.** We also conducted a systematic analysis of the effects of fluorophore-coupled protein concentration as well as NR length and width on the presence and the degree of *FINE*. In the top panels of Fig. 4, the 3D contour plots show the typical spatial and temporal profiles of biomolecular emission from 1 μg/mL (A), 5 μg/mL (B), and 200 μg/mL (C) DTAF-antiIgG

measured along the long axis of individual L-ZnO NRs of similar lengths. As seen in all three plots, the phenomenon of *FINE* was present from all cases and the magnitudes of the raw fluorescence intensities on both $NR_{ef}$ and $NR_{sf}$ increased with higher protein concentrations. The fluorescence data in Fig. 4(A through C) also indicate that the degree of *FINE* is dependent on the protein concentration. The $(\boldsymbol{I}_{avg,NR_{ef}} - \boldsymbol{I}_{avg,NR_{sf}})/\boldsymbol{I}_{avg,NR_{sf}}$ values increased approximately from 35.7% (A), 66.7% (B), to 87.5% (C).

**NR Length/Width on *FINE*.** Further, within each concentration level, ZnO NRs of varying lengths and widths were examined to elucidate any relationship between the physical dimensions of the NR and the degree of *FINE*. We plotted the difference in the normalized and averaged fluorescence intensity between $NR_{ef}$ and $NR_{sf}$, $\boldsymbol{\Delta I} = \boldsymbol{I}_{avg,NR_{ef}} - \boldsymbol{I}_{avg,NR_{sf}}$, as a function of the NR length and width for the biomolecular treatment of 1 μg/mL (D), 5 μg/mL (E), and 200 μg/mL (F) DTAF-antiIgG. In all protein concentration cases we tested, the degree of *FINE* was measured to be larger as the NR length becomes longer, as displayed in Fig. 4(D through F). On the other hand, we did not observe any significant effect of ZnO NR width, within the range of diameters presented in Fig. 2(C), on $\boldsymbol{\Delta I}$, regardless of the concentration.

When increasing the protein concentration for the similar length NRs in Fig. 4(A through C), both $\boldsymbol{I}_{avg,NR_{ef}}$ and $\boldsymbol{I}_{avg,NR_{sf}}$ values are expected to become larger while leaving the ratio of $\boldsymbol{I}_{avg,NR_{ef}} / \boldsymbol{I}_{avg,NR_{sf}}$ unaffected since the amount of proteins will increase both on $NR_{ef}$ and $NR_{sf}$ facets. For the scenarios of increased NR lengths with the same protein concentration in Fig. 4(D through F), the larger surface footprint across the NR main body relative to the NR end facets is anticipated to yield higher $\boldsymbol{I}_{avg,NR_{sf}}$ with little change in $\boldsymbol{I}_{avg,NR_{ef}}$ which will reduce the degree of *FINE*. Yet, the degree of *FINE* was found to increase with longer NR lengths from our experiments. The higher degree of *FINE* seen with increasing protein concentrations and increasing NR length represented in Fig. 4 cannot be straightforwardly explained by the potentially higher amounts of proteins bound on ZnO NRs. Similar to what we discussed in the section of Occurrence Frequency and Possible Origins of *FINE*, this is another indication that the amount of proteins adsorbed onto the NR surface does not seem to be a definitive indicator in gauging the degree of *FINE*. We, therefore, turned to computer simulations to

gain further insights into this observation. Our simulation results indicate that, even for the same single emitter, the physical characteristics of the NR, pertaining mainly to the reduced dimensions and high shape anisotropy, allow for better propagation of guided light for longer rods than for shorter rods and contribute to higher levels of *FINE*. This aspect will be discussed shortly in detail in Fig. 7.

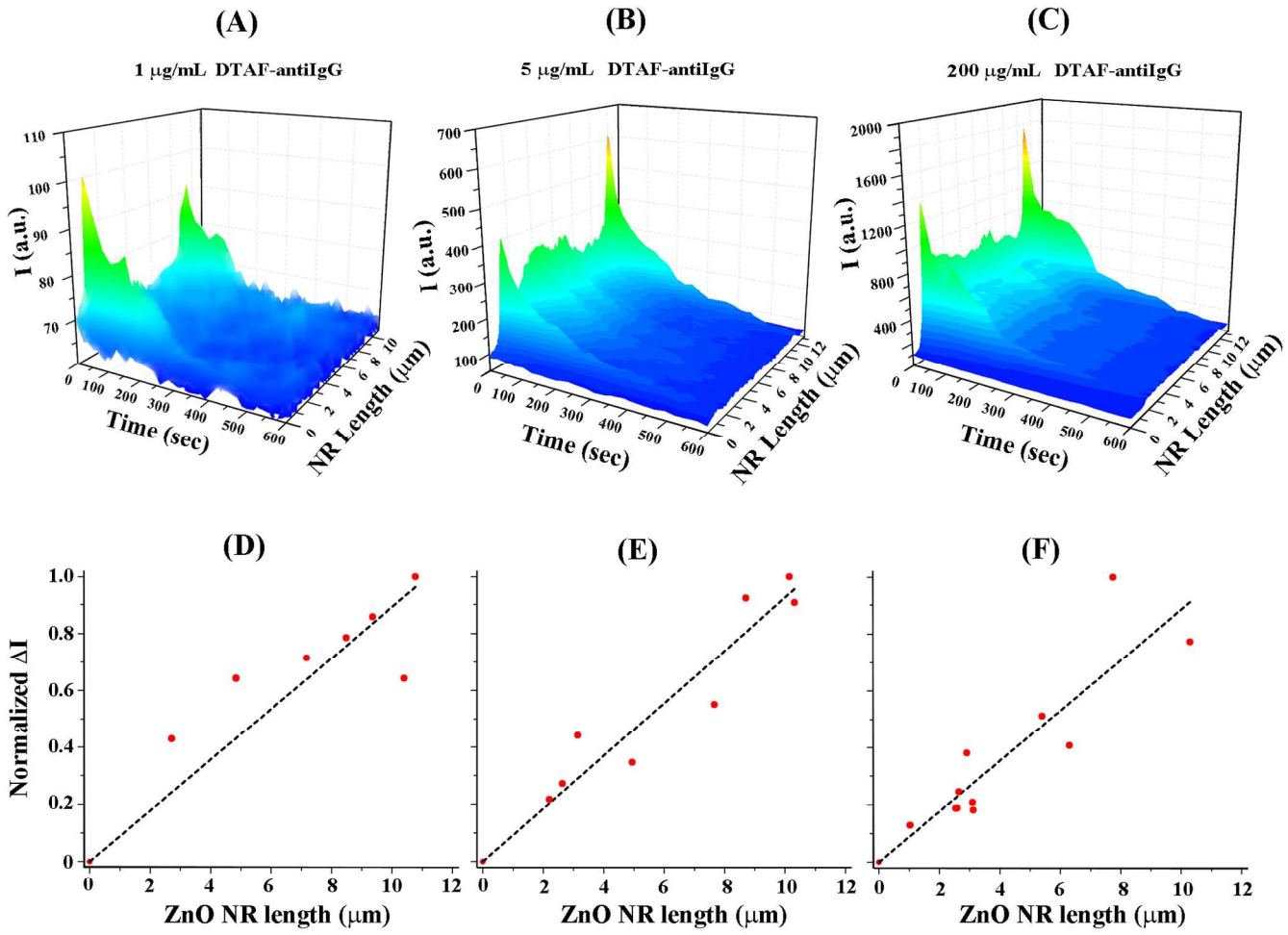


**Figure 4.** **(A-C)** Effect of protein concentration on the degree of *FINE*. 3D contour plots on the top display the typical spatial and temporal profiles of fluorescence of 1 μg/mL (A), 5 μg/mL (B), and 200 μg/mL (C) DTAF-antiIgG measured along the long axis of individual ZnO NRs of a similar length. The phenomenon of fluorescence intensification on NR ends is apparent from all cases. **(D-F)** Effect of NR

length on the degree of *FINE*. ZnO NRs of various lengths and widths were analyzed after treating them with the same biomolecular deposition condition of 1 μg/mL (D), 5 μg/mL (E), and 200 μg/mL (F) DTAF-antiIgG. For each concentration level, the degree of *FINE* was characterized by plotting normalized $\Delta I$ ($I_{avg,NR_{ef}} - I_{avg,NR_{sf}}$), with respect to the NR length. The dotted lines in the normalized $\Delta I$ plots were inserted to guide the eye. For all protein concentrations, the degree of *FINE* is measured to be larger as the NR length becomes longer.

**FDTD Simulations.** We have also carried out finite-difference time-domain (FDTD) simulations in order to probe the electromagnetic field intensities and distributions contributing to the experimentally observed *FINE* phenomenon from TRITC-antiIgG and DTAF-antiIgG adsorbed onto single ZnO NRs.

**Near-Field Emission Depending on the Dipole Polarization and Location on a NR.** Fig. 5 displays the FDTD results obtained when a dipole, radiating at 576 nm to model the emission of TRITC-antiIgG, is located in the middle (A) and at the end (B) of the ZnO NR, exemplifying the two cases of the fluorophore emission from the main body and end facets of a ZnO NR, respectively. The two positional scenarios are simulated for three polarized dipole cases: perpendicular (top), transverse (middle), and parallel (bottom) to the long axis of the ZnO NR.

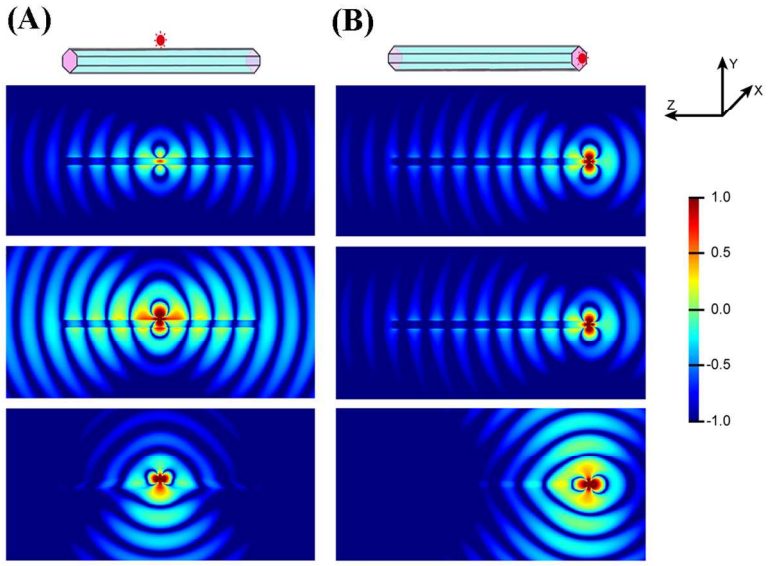


**Figure 5.** FDTD simulations showing radiation energy flows from a fluorophore placed in the middle (A) and at the end (B) of a ZnO NR by considering a single emitter radiating at 576 nm as a model system for TRITC-antiIgG. The radiation patterns are obtained from a dipole polarized along the X- (top), Y- (middle), and Z- (bottom) direction. **(A)** For the fluorophore located in the middle of the NR, a dipole polarization in the X-direction resulted in moderate coupling of the radiation energy to the NR. When the dipole was polarized in the Y-direction, almost all the energy was coupled into the underlying NR and led to the formation and propagation of very strong evanescent waves before finally being radiated out from the $NR_{ef}$. When the dipole was polarized along the Z-direction, only a very small portion of the dipole radiation was coupled into the NR. **(B)** For a TRITC-antiIgG dipole placed on the ZnO NR end facet, dipoles polarized in the X- and Y-directions resulted in strong coupling of the radiation energy to the NR with equally high efficiency. When the dipole was polarized along the Z-direction, only a very small portion of the dipole radiation was coupled into the NR as was also seen for the earlier case.

When a dipole was positioned in the middle of the ZnO NR provided in Fig. 5(A), our FDTD simulation results indicated that emission from both the X- and Y-polarized cases could be readily

coupled into the NR body. However, unlike the strong emission coupling of the Y-polarized dipole, the X-polarized case yielded approximately an order of lower coupling efficiency. By contrast, the Z-polarized dipole case did not show much interaction with the NR. When the dipole was placed at the end of the ZnO NR instead, the FDTD simulation panels shown in Fig. 5(B) revealed that emission from both the cases of X-and Y-polarization could strongly couple into the NR body equally efficiently. The coupled radiation led to the formation and propagation of very strong evanescent waves before finally being radiated out from the NR ends. Emission from the Z-polarized case interacted only weakly with the NR just as the case of the fluorophore placed in the middle of the NR.

Our experimental conditions can be viewed as a system with multidirectional electric dipoles placed on different crystal facets exposed on a ZnO NR. Hence, the experimental results should encompass all of the dipole location and polarization cases presented in Fig. 5. When considering these simulation results in combination, radiation emitted from fluorophores bound on the main body of a ZnO NR is predominantly from only the fluorophores located at those sites. In contrast, radiation emitted from the NR end facets has contributions from all of the fluorophores on the surface of the ZnO NR through various radiation coupling and evanescent wave-guiding pathways. Therefore, when considering various scenarios of fluorophore locations and polarizations on a ZnO NR collectively, the simulation results also corroborate the experimental observations. As effective dipole emission coupling into the ZnO NR body reduces the radiation energy directly emitted to far-field from the dipole location and instead, leads to radiation propagation along the NR long axis for subsequent far-field emission from the NR ends, the phenomenon of *FINE* may be readily observed from the ZnO NR platform.

**Far-field Radiation Depending on the Dipole Wavelength and the Presence of a ZnO NR Medium.** We also performed 3D electrodynamic simulations to further elucidate the underlying coupling mechanism between the different fluorophore/ZnO NR systems contributing to the experimentally observed *FINE* phenomenon. An isolated electric dipole radiating at 517 nm for DTAF-antiIgG's emission is provided in Fig. 6(A) to display the torus-like radiation pattern emanating outwards in the plane perpendicular to the dipole orientation when no medium is coupled with the dipole. Unlike this

uniformly distributed emission of the electric dipole in free space, the radiation patterns of a dipole placed 10 nm away from a ZnO NR surface in Figs. 6(B and C) are markedly affected by the physical characteristics of the underlying NR. As displayed in Fig. 6(B), the radiation pattern of the 517 nm dipole displays more of a dumbbell-like 3D pattern propagating along the long axis of the ZnO NR. In this simulation, only the dipole polarization case oriented perpendicular to the ZnO NR surface was considered since this configuration led to the largest degree of coupling, as was described in Fig. 5. The 3D radiation pattern was prominently suppressed at the origin in the X-direction, while there was significant enhancement in the Y-direction. The reduced dimensions and high anisotropy of the proximate ZnO NR influenced the intrinsic emission behavior of the nearby oscillating dipole. Additionally, to probe the effect of wavelength on this coupling behavior, Fig. 6(C) illustrates the emission pattern from an electric dipole radiating at 576 nm modeling the case of TRITC-antiIgG's emission. Similar to the 517 nm dipole, there was a dumbbell-like pattern propagating along the Y-axis, however, the degree of guided radiation varied. For the specified NR dimensions used in the simulation, a slightly better directional coupling along the ZnO NR was seen for the 517 nm dipole relative to the 576 nm dipole.

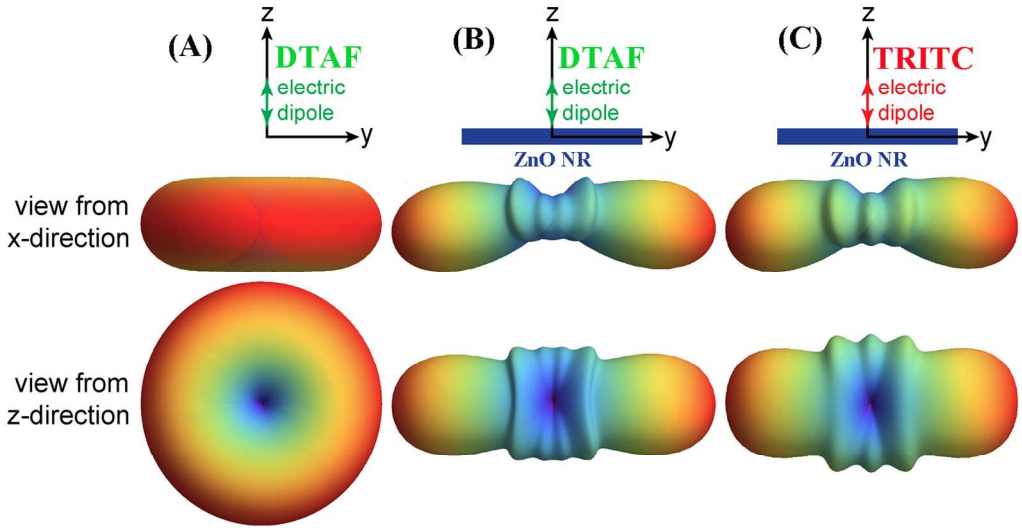

**Figure 6.** Radiation patterns of an isolated electric dipole in vacuum and an electric dipole of different emission wavelengths coupled with a ZnO NR. The ZnO NRs modeled in (B and C) both have the diameter and length of 100 nm and 2.5 μm, respectively, and are oriented along the Y-axis as shown in the schematic. The electric dipole considered in (A-C) is polarized along the Z-axis, and the distance between the electric dipole and the ZnO NR is 10 nm to account for protein conjugation. **(A)** Far-field radiation pattern of an isolated electric dipole with radiation (emission) wavelength of 517 nm in the absence of a ZnO NR medium. **(B and C)** Far-field radiation patterns of an electric dipole located in the middle of the same ZnO NR. The radiation (emission) wavelengths of the dipoles in (B) and (C) are 517 nm and 576 nm, respectively.

**Far-Field Radiation Patterns Depending on the NR Physical Dimensions.** To further elucidate the relationship between the physical dimensions of the ZnO NR and the coupling behavior of the electric dipole, the influence of NR length and width was evaluated via computer simulations, and the results are summarized in Fig. 7. The same configuration used earlier is displayed in Fig. 7(A) to serve as a reference for probing the effect of NR dimensional changes on the electromagnetic radiation pattern of a 517 nm dipole. The evaluated physical dimensions of NRs in Fig. 7(B through D) are 2.5 μm in length / 100 nm in diameter (B), 10 μm/100 nm (C), and 2.5 μm/500 nm (D). A pair of far-field patterns is shown in Fig. 7(B-D) for each NR, where the top (and bottom) simulations correspond to the spatial patterns observed from the Z-axis (and X-axis). Fig. 7(B) displays the far-field radiation patterns from the 517 nm dipole placed 10 nm away from the surface of a ZnO NR exhibiting an aspect ratio of 25:1 (length:width). In Fig. 7(C), the NR width was held constant and the NR length was increased by a factor of 4 when compared to the NR in Fig. 7(B). The use of a longer NR in Fig. 7(C) revealed more prominent and highly directional emission behavior along the NR long axis when compared to the results shown in Fig. 7(B). By contrast, when the NR length from Fig. 7(B) was held constant and the

width of the NR was increased by a factor of 5, the far-field radiation pattern became more complex with less directionality as seen in Fig. 7(D). In this case, the energy was radiated into several directions with a relatively small solid angle. The simulations corroborate the experimentally observed trend of an increased degree of *FINE* for longer rods at each concentration level of DTAF-antiIgG assayed. Further, experimentally, we did not observe any correlation between variations in width and the degree of *FINE*.

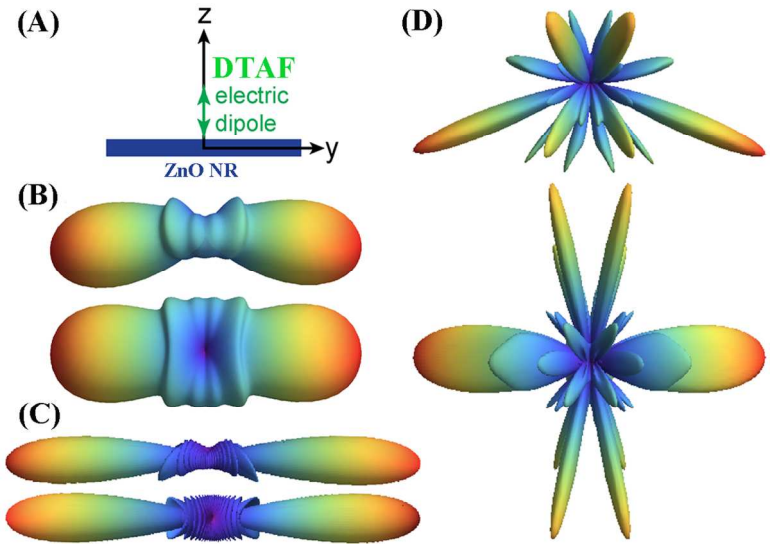


**Figure 7. (A)** The schematic illustrates an electric dipole with a wavelength of 517 nm polarized along the Z-axis placed in the middle of a ZnO NR lying along the Y-axis. The distance between the electric dipole and the ZnO NR is kept the same as before, 10 nm. **(B-D)** Far-field radiation patterns of a 517 nm electric dipole located in the middle of a ZnO NR. The radiation patterns in (B-D) are obtained by simulating ZnO NRs of different lengths/diameters: (B) 2.5 μm/100 nm, (C) 10 μm/100 nm, and (D) 2.5 μm/500 nm. A pair of far-field patterns is shown for each NR where the top (and bottom) simulations correspond to the spatial patterns observed from the Z-axis (and X-axis).

## SUMMARY

In summary, we provide much needed insights into the origin and mechanism of *FINE* previously identified from individual ZnO NRs coupled with fluorophore-tagged biomolecules. We have systematically profiled the key factors affecting the intriguing optical behavior of *FINE* from individual ZnO NRs by examining the effect of the NR length, width, and orientation as well as the protein concentration and fluorophore's spectroscopic property on the presence, degree, and temporal stability of *FINE*. We consistently observed highly localized intensification of fluorescence signal on the ZnO $NR_{ef}$ relative to the signal collected along the $NR_{sf}$ and confirmed the presence of *FINE* from all our measurement cases consisting of varying NR physical dimensions, orientations, and fluorophore types. The degree of *FINE* was found to be dependent on the NR orientation, NR length, and protein concentration. The measured degree of *FINE* was highly pronounced for V-ZnO NRs relative to L-ZnO NRs. Additionally, the degree of *FINE* on ZnO NRs was increased in magnitude for longer NRs and for higher protein concentrations. Temporally, the biomolecular emission signal on the ZnO $NR_{ef}$ persisted much longer relative to the photostability of the signal derived from the $NR_{sf}$ when comparing the time-dependent decay of fluorescence intensity measured from the end facets versus side facets of individual ZnO NRs consisting of different orientations and physical dimensions decorated with different fluorophore types. Further FDTD simulations, taking into account various scenarios of dipole polarizations, emission wavelengths, locations on the NR, and NR physical dimensions, also corroborated our experimental observations of each factor on the presence and the degree of *FINE*. We anticipate our efforts will encourage innovative applications exploiting the highly directional, localized and enhanced *FINE* in single ZnO NR-based biodetection as well as provide an understanding for signal interpretation of fluorescence-based applications employing ensembles of vertically oriented ZnO NRs.

**ACKNOWLEDGEMENTS**

The authors acknowledge financial support on this work by the National Institutes of Health, National Research Service Award (1R01DK088016) from the National Institute of Diabetes and Digestive and Kidney Diseases.

## References


1. M. C. Morris, *Fluorescence-Based Biosensors: From Concepts to Applications*, Elsevier Science, Waltham, MA, 2012.
2. R. B. Thompson, *Fluorescence Sensors and Biosensors*, CRC Press, Boca Raton, FL, 2005.
3. A. Dorfman, N. Kumar and J. Hahm, *Langmuir*, 2006, **22**, 4890-4895.
4. A. Dorfman, N. Kumar and J. Hahm, *Adv. Mater.*, 2006, **18**, 2685-2690.
5. K. Aslan, I. Gryczynski, J. Malicka, E. Matveeva, J. R. Lakowicz and C. D. Geddes, *Curr. Opin. Biotechnol.*, 2005, **16**, 55-62.
6. K. Aslan, J. R. Lakowicz and C. D. Geddes, *Anal. Bioanal. Chem.*, 2005, **382**, 926-933.
7. J. R. Lakowicz, *Anal. Biochem.*, 2001, **298**, 1-24.
8. J. R. Lakowicz, C. D. Geddes, I. Gryczynski, J. Malicka, Z. Gryczynski, K. Aslan, J. Lukomska, E. Matveeva, J. Zhang, R. Badugu and J. Huang, *J. Fluoresc.*, 2004, **14**, 425-441.
9. X. X. Han, Y. Kitahama, Y. Tanaka, J. Guo, W. Q. Xu, B. Zhao and Y. Ozaki, *Anal. Chem.*, 2008, **80**, 6567-6572.
10. N. Kumar, A. Dorfman and J.-i. Hahm, *Nanotechnology*, 2006, **17**, 2875-2881.
11. J. Hahm, in *Metal-enhanced Fluorescence*, ed. C. D. Geddes, John Wiley & Sons, Inc., Hoboken, NJ, 2010, ch. 12, pp. 363-391.
12. J. Hahm, *J. Nanosci. Nanotech.*, 2014, **14**, 475-486.
13. V. Adalsteinsson, O. Parajuli, S. Kepics, A. Gupta, W. B. Reeves and J. Hahm, *Anal. Chem.*, 2008, **80**, 6594-6601
14. A. Dorfman, O. Parajuli, N. Kumar and J. Hahm, *J. Nanosci. Nanotech.*, 2008, **8**, 410-415.
15. J. Hahm, *J. Biomed. Nanotech.*, 2013, **9**, 1-25.
16. W. Hu, Y. Liu, H. Yang, X. Zhou and C. M. Li, *Biosens. Bioelectron.*, 2011, **26**, 3683-3687.
17. A. B. Dahlin, *Sensors*, 2012, **12**, 3018-3036.
18. J. H. Luong, K. B. Male and J. D. Glennon, *Biotechnol. Adv.*, 2008, **26**, 492-500.
19. M. R. Melo, S. Clark and D. Barrio, *Clin. Chem. Lab. Med.*, 2011, **49**, 581-586.

20. C. Wingren and C. A. Borrebaeck, *Drug Discov. Today*, 2007, **12**, 813-819.

21. R. Yan, J.-H. Park, Y. Choi, C.-J. Heo, S.-M. Yang, L. P. Lee and P. Yang, *Nat. Nanotech.*, 2012, **7**, 191-196.

22. J. Tang and R. A. Marcus, *J. Chem. Phys.*, 2005, **123**, 204511-204516.

23. D. Ratchford, K. Dziatkowski, T. Hartsfield, X. Li, Y. Gao and Z. Tang, *Appl. Phys. Lett.*, 2011, **109**, 103509.

24. M. Singh, S. Song and J. I. Hahm, *Nanoscale*, 2014, **6**, 308-315.

25. H. Morkoç and Ü. Özgür, *Zinc Oxide: Fundamentals, Materials and Device Technology*, Wiley-VCH Verlag GmbH & Co., Weinheim, Germany, 2009.

26. S. R. Sakamoto, C. Ozturk, Y. T. Byun, J. Ko and N. Dagli, *IEEE Photonics Technol. Lett.*, 1998, **10**, 985-987.

27. D. J. Gargas, M. C. Moore, A. Ni, S.-W. Chang, Z. Zhang, S.-L. Chuang and P. Yang, *ACS Nano*, 2010, **4**, 3270-3276.

28. D. J. Sirbuly, M. Law, H. Yan and P. Yang, *J. Phys. Chem. B*, 2005, **109**, 15190-15213.

29. J. C. Johnson, H. Yan, R. D. Schaller, L. H. Haber, R. J. Saykally and P. Yang, *J. Phys. Chem. B*, 2001, **105**, 11387-11390.

30. J. C. Johnson, H. Yan, P. Yang and R. J. Saykally, *J. Phys. Chem. B*, 2003, **107**, 8816-8828.

31. H. Chanzy, B. Henrissat and R. Vuong, *FEBS Lett.*, 1984, **172**, 193-197.

32. J. Lehtio, J. Sugiyama, M. Gustavsson, L. Fransson, M. Linder and T. T. Teeri, *Proc. Natl. Acad. Sci.*, 2003, **100**, 484-489.

33. X. Gao, L. Yang, J. A. Petros, F. F. Marshall, J. W. Simons and S. Nie, *Curr. Opin. Biotechnol.*, 2005, **16**, 63-72.

34. A. Margineanu, J. Hofkens, M. Cotlet, S. Habuchi, A. Stefan, J. Qu, C. Kohl, K. Müllen, J. Vercammen, Y. Engelborghs, T. Gensch and F. C. De Schryver, *J. Phys. Chem. B*, 2004, **108**, 12242-12251.

35. L. Song, E. J. Hennink, T. Young and H. J. Tanke, *Biophys. J.*, 1995, **68**, 2588-2600.

## Graphical Abstract